Mon. Not. R. Astron. Soc. **326,** 578–596 (2001)

H I observations of interacting galaxy pair NGC 4038/9

Scott Gordon,[1★] Bärbel Koribalski[2] and Keith Jones[1]

[1]*Department of Physics, University of Queensland, St. Lucia, Brisbane, QLD 4072, Australia*

[2]*Australia Telescope National Facility, CSIRO, PO Box 76, Epping, NSW 1710, Australia*

Accepted 2001 April 11. Received 2001 April 10; in original form 2000 November 14

ABSTRACT

We present the results of new radio interferometer H I line observations for the merging galaxy pair NGC 4038/9 ('The Antennae'), obtained using the Australia Telescope Compact Array. The results improve substantially with respect to those of van der Hulst and show in detail the two merging galactic discs and the two tidal tails produced by their interaction. The small edge-on spiral dwarf galaxy ESO 572–G045 is also seen near the tip of the southern tail, but distinct from it. It shows no signs of tidal interaction. The northern tidal tail of the Antennae shows no H I connection to the discs and has an extension towards the west. The southern tidal tail is continuous, with a prominent H I concentration at its tip, roughly at the location of the tidal dwarf galaxy observed optically by Mirabel, Dottori & Lutz. Clear velocity structure is seen along the tidal tails and in the galactic discs. Radio continuum images at 20 and 13 cm are also presented, showing the discs in detail.

Key words: galaxies: individual: NGC 4038 – galaxies: individual: NGC 4039 – galaxies: individual: ESO 572–G045 – galaxies: interactions – radio continuum: galaxies – radio lines: galaxies.

1 INTRODUCTION

The Antennae (NGC 4038/4039 = Arp 244, see Fig. 1) are a pair of closely interacting disc galaxies in the advanced stages of merging, named after the appearance of the two spectacular galactic tails produced by gravitational tidal forces during the interaction. There are a number of similar systems known, including 'The Mice' (NGC 4676A/B) described by Hibbard (1995) and 'The Superantennae' (IRAS 19254–7245) described by Mirabel, Lutz & Maza (1991). Also visible to the south-west of the southern tail of the Antennae is the edge-on spiral dwarf galaxy ESO 572–G045 (Fig. 1), which has no measured optical velocity. Some parameters of the Antennae and ESO 572–G045 are given in Table 1.

On a large scale, the Antennae appear roughly symmetrical, although the southern tail is more prominent both optically (Fig. 1) and in H I (van der Hulst 1979; this paper). The two galaxies retain distinct nuclei as seen from optical and CO observations. However, the galactic discs, while still present, are colliding and have severely disrupted one another. The two nuclei are currently ~1.13 arcmin or ~6.3 kpc apart across the line of sight, according to CO measurements by Stanford et al. (1990). As a result of the collision, vigorous star formation is occurring in the discs and in the overlap region between them. This is evidenced by a variety of data, for example by the *HST* optical observations (Whitmore & Schweizer 1995; Whitmore et al. 1999), and the *ISO* infrared observations (e.g. Vigroux et al. 1996) which show a high infrared luminosity in the two nuclei and particularly in the overlap region.

The tidal tails, disturbed structure, and star formation are all classic features of interacting galaxies. Given this and the closeness of the system ($D = 19.2$ Mpc[1]), the Antennae have attracted a lot of attention in observational and theoretical studies of galaxy interaction.

1.1 History of the Antennae

The Antennae were first seen by C.O. Lampland of the Lowell Observatory in 1917 (Parker 1990), and were later described by Shapley & Paraskevopoulos (1940) and Minkowski (1957), who identified the pair with a radio source and first described them as interacting galaxies. They were also noted as number 244 in the Arp atlas of peculiar galaxies (Arp 1966).

Systems resembling the Antennae were produced in the pioneering computer modelling simulations by Toomre & Toomre (1972), providing the first theoretical proof that features such as galactic tails were produced by gravitational tides between interacting galaxies, leading to much of the present understanding of their evolution. Clutton-Brock (1972) published work similar to the Toomres', but less extensive. The Antennae are the first or the 'earliest' of the 11 systems in the 'Toomre Sequence' (Toomre

★E-mail: gordon@physics.uq.edu.au

[1] This paper assumes a Hubble constant of $H_0 = 75\,\mathrm{km\,s^{-1}\,Mpc^{-1}}$ and a velocity relative to the Local Group of $1439\,\mathrm{km\,s^{-1}}$ for the Antennae (Whitmore & Schweizer 1995 from de Vaucouleurs et al. 1991) giving a Hubble distance of 19.2 Mpc and a linear scale of 1 arcmin ≈5.6 kpc.

Table 1. Properties of NGC 4038/9 ('The Antennae') and ESO 572–G045.

Name	J2000 position RA	DEC	Optical velocity (heliocentric)	$B_T^{o\,(*)}$	Galaxy type
NGC 4038	$12^h01^m52.8^{s(1)}$	$-18°52'05''^{(1)}$	$1663 \pm 20\,km\,s^{-1(2)}$	$10.59^{(2)}$	$SB(s)m(pec)^{(2)}$
NGC 4039	$12^h01^m53.6^{s(1)}$	$-18°53'12''^{(1)}$	$1655 \pm 28\,km\,s^{-1(2)}$	$10.69^{(2)}$	$SA(s)m(pec)^{(2)}$
ESO 572–G045	$12^h01^m09.4^{s(3)}$	$-19°04'49''^{(3)}$	unknown		$Scd^{(3)}$

Linear distance scale ($D = 19.2$ Mpc) : 1 arcmin ≈5.6 kpc.
$^{(*)}$ The photoelectric total magnitude, corrected for galactic and internal absorption, and redshift. Refer to $^{(2)}$.
$^{(1)}$ Stanford et al. (1990).
$^{(2)}$ de Vaucouleurs et al. (1991).
$^{(3)}$ Karachentsev et al. (1993).

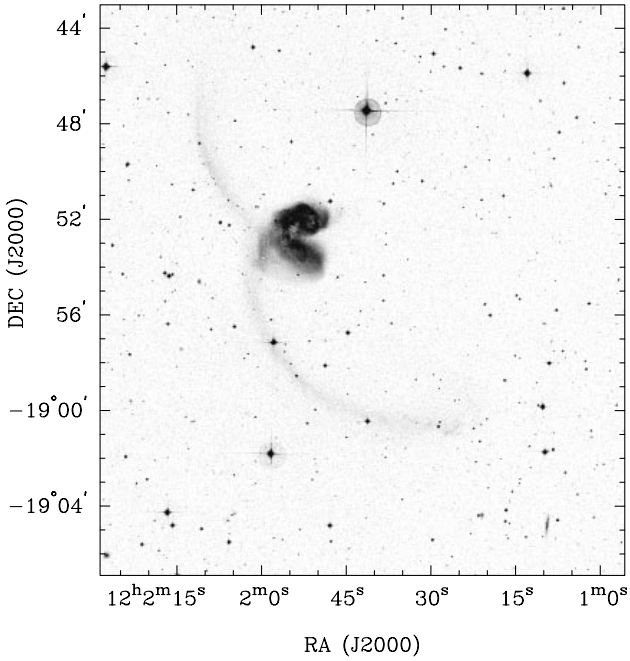

Figure 1. Digitised Sky Survey (DSS) optical image of the Antennae (NGC 4038/9).

1977), and are still used for modelling (e.g. Barnes 1988; Mihos, Bothun & Richstone 1993). Collectively, these simulations have disproved, for most interacting systems, earlier explanations for galactic pairs and interaction effects, such as the suggestion by Arp (1969) that when two galaxies of different sizes were interacting, the smaller one was an ejected component of the larger.

1.2 Previous observations

Observations of the Antennae have been made at many radio, infrared, optical, and X-ray wavelengths, including many emission lines such as Hα (Amram et al. 1992), [C II] (Nikola et al. 1998), CO J = 1–0 (Sanders & Mirabel 1985; Stanford et al. 1990; Young et al. 1995; Gao et al. 1998; Wilson et al. 2000; Gao et al. 2001), and H I (Huchtmeier & Bohnenstengel 1975; van der Hulst 1979), Hα, Hβ, [O I], [O III], He I and [S II] (Rubin, Ford & D'Odorico 1970), and also radio continuum (Condon 1983, 1987; Hummel & van der Hulst 1986).

More recently, radio observations of the Antennae have been made using the Very Large Array (VLA). These include high-resolution 6-cm and 3.5-cm observations by Neff & Ulvestad (2000), and H I observations by Mahoney, Burke & van der Hulst (1987) and by Hibbard, van der Hulst & Barnes (in preparation).

Infrared continuum studies have been made using the *ISO* satellite by Fischer et al. (1996), Kunze et al. (1996), Vigroux et al. (1996) and Mirabel et al. (1998). X-ray studies have been made using the Einstein Observatory by Fabbiano & Trinchieri (1983), *ROSAT* by Read, Ponman & Wolstencroft (1995) and Fabbiano, Schweizer & Mackie (1997), *ASCA* by Sansom et al. (1996), and most recently using *Chandra* by Fabbiano, Zezas & Murray (2000).

1.3 The inner discs

There are numerous H II regions distributed in a ring in the NGC 4038 (northern) disc and a few also along an arc in the NGC 4039 (southern) disc. The shape of their distribution is roughly that of the letter 'e', and is seen clearly as knots, or compact objects, in blue optical images as well as in Hα (Amram et al. 1992) and in the radio continuum (Hummel & van der Hulst 1986). The *Hubble Space Telescope* resolved the H II regions into many groups and clusters of young stars, with over 700 mostly blue compact objects 20–30 pc wide (Whitmore & Schweizer 1995; Whitmore et al. 1999).

The location of one particular group of optical and radio continuum knots in the overlap region between the two galactic discs, combined with the youth of the stars, suggests that this star formation activity is caused by the ongoing interaction. Further high-resolution mid-infrared studies using the *ISO* satellite (Mirabel et al. 1998) show the strongest star formation in the overlap region, accounting for half of the 15 μm flux, rather than in the more optically spectacular star-forming ring. This is explained as a result of obscuration by the large quantity of dust, which tends to hide star-forming regions at optical wavelengths but also makes them highly visible in the infrared (Kunze et al. 1996; Mirabel et al. 1998; Wilson et al. 2000). Wilson et al. (2000) produced detailed CO maps and molecular mass estimates for the disc region using the Caltech mm-array. The maps show seven giant molecular cloud complexes, including the two nuclei and five complexes in the disc overlap region which have ongoing massive star formation. Gao et al. (2001) made a similar study combining single-dish and interferometric observations, leading to an estimated molecular gas mass of $1.38 \times 10^{10}\,M_\odot$ (adopting $D = 19.2$ Mpc), implying a modest star formation efficiency.

1.4 Southern-tail tidal dwarf galaxy

At the tip of the southern tail is an object thought to be a dwarf galaxy formed from material ejected from the galactic discs during the interaction (Mirabel et al. 1992). It contains many hot, young stars, and coincides with a major concentration of H I which has been noted in earlier studies (van der Hulst 1979).

Table 2. Details of the radio observations.

Instrument	ATCA
Array configurations	6C (1996 July 24); 1.5A (1996 Oct 25); 750A (1996 Nov 12, 13); 375 (1998 Mar 28)
Baseline coverage	30.6–6000 m, 75 baselines (56 unique)
Pointing centre	RA $= 12^{h}01^{m}40^{s}$, Dec $= -18°55'00''$
Frequency configuration	IF1 (20 cm): centre 1413 MHz, bandwidth 8 MHz, 512 channels, 2 polarizations
	IF2 (13 cm): centre 2378 MHz (6C, 1.5A, 750-A arrays) or 2496 MHz (375 array)
	bandwidth 128 MHz, 32 channels, 4 polarizations
Primary beam FWHM	33 arcmin (IF1 or 20 cm), 21 arcmin (IF2 or 13 cm)
Observing time per run	11–12 h overall; ~8.5–9.5 h on source (3.8/2.3 h for second 750-A run)
Total observing time	50 h overall; 39 h on source
Flux calibration	10 min per run, using PKS 1934–638 (14.88 Jy in IF1, 11.5 Jy in IF2)
Phase calibration	alternately 30 min on source, 3 min on PKS 1151–348 (6.1/4.1 Jy) or 1127–145 (5.0/4.65 Jy)
Calibrated bandwidth	IF1 (20 cm): 6.8 MHz (1436 km s^{-1} as H I); IF2 (13 cm): 100 MHz
Image Weight; rms noise; beam	H I : 'robust = 1'; 1.0 mJy beam^{-1} versus 0.95 mJy beam^{-1} theoretical; 42 arcsec beam
	20 cm : 'uniform'; 0.23 mJy beam^{-1} versus 0.25 mJy beam^{-1} theoretical; 16 arcsec beam
	13 cm : 'uniform'; 0.056 mJy beam^{-1} versus 0.039 mJy beam^{-1} theoretical; 9.5 arcsec beam

This dwarf is of particular interest because it matches the results of computer modelling, confirming that tidally disturbed material can become concentrated enough to form bound objects (Barnes & Hernquist 1992, 1996). Additionally, observing a dwarf galaxy soon after its formation could shed light on the origin and star-forming properties of such galaxies, about which little is currently known.

Section 2 describes the observations and data reduction. This is followed by a summary of the major features in Section 3. The implications of the data, and its relationship to the previous work, is given in Section 4. Finally, Section 5 presents a summary of our new and interesting results.

2 OBSERVATIONS AND DATA REDUCTION

We have observed the Antennae group using the Australia Telescope Compact Array (ATCA)[2], a linear east–west oriented radio interferometer with six 22-m parabolic dishes. Table 2 gives details of the observations. In total, four successful 12-h observations were obtained (plus one additional 2–3 − h run) using different antenna arrays chosen to give baselines spread across a range as wide as possible. The dual 20/13 cm feedhorns on the ATCA, producing two independent IFs, were used to observe in both bands simultaneously. Data reduction was performed, unless otherwise stated, using the MIRIAD analysis package (Sault, Teuben & Wright 1995). All radio images presented have been corrected for the primary-beam attenuation. In some figures, pixels below 3σ have been masked out prior to correction to exclude noise. All velocities are in the heliocentric reference frame and the 'optical' definition is $v = c(\Delta\lambda/\lambda_0)$. The measured H I velocities have an uncertainty of about 5 km s^{-1}. Positions are expressed in the J2000 system, including any from other papers.

2.1 H I line and 20-cm continuum observations

The 20-cm data (IF1; see Table 2) covered the redshifted H I emission line of neutral atomic hydrogen, plus some continuum channels to each side. The data were Hanning-smoothed to a resolution of ~6.6 km s^{-1}. Channels at each edge of the passband (attenuated by 50 per cent or more) were removed, giving a remaining bandwidth of ~6.8 MHz. This band was used to produce separate H I line and 20-cm continuum data sets, using a first-order polynomial (or baseline) fit to the line-free channels for each side of the spectrum.

The 20-cm (1413 MHz) flux for PKS 1934–638 is ~14.88 Jy. The derived antenna gains ranged from 0.99 to 1.06, indicating a typical ~3–4 per cent change during calibration.

The line data for the individual observations were then combined and Fourier transformed to produce a spectral image cube. The visibilities were weighted using 'robust' weighting with the robustness parameter equal to one, chosen to give a good compromise between sensitivity and resolution. This image cube was cleaned by deconvolution using a combined Högbom/Clark/Steer algorithm (Högbom 1974; Clark 1980; Steer, Dewdney & Ito 1984). The H I maps have a channel width of 10 km s^{-1}; the pixel size is 5×5 arcsec^2. The rms residual after cleaning is ~1 mJy beam^{-1}. The map was restored using a circular restoring beam of 42 arcsec.

The AIPS task MOMNT was used to produce maps of H I integrated intensity (moment-0), intensity-weighted mean velocity (moment-1) and velocity dispersion (moment-2). To smooth the cube spatially and in velocity we used a 3 pixel 'boxcar' function and a five channel 'Hanning' function, respectively. A lower flux cut-off of 2.1 mJy beam^{-1} (~3σ after smoothing) was applied.

The 20-cm continuum map (see Fig. 7a later) was made using 'uniform' weighting resulting in a noise after cleaning of the 0.23 mJy beam^{-1}, and a 16 arcsec restoring beam was used.

2.2 13-cm continuum observations

The 13-cm data (IF2; see Table 2) had 128-MHz bandwidth and full polarization information. After excluding edge channels, the bandwidth was 100 MHz. No polarization was observed above 1 per cent.

The 13-cm continuum map (see Fig. 7b later) was made using 'uniform' weighting, resulting in a noise after cleaning of the 0.056 mJy beam^{-1} using a 9.5 arcsec restoring beam.

The flux of PKS 1934–638 ranges from ~11.5 Jy at 2378 MHz to ~11.1 Jy at 2496 MHz. The derived antenna gains ranged from 0.99 to 1.05, giving a typical change during calibration of ~3 per cent.

3 RESULTS

3.1 H I channel map summary

Neutral hydrogen in the Antennae group is observed in the velocity range of ~1340–1946 km s^{-1} (see Fig. 8, later). At low velocities the H I emission consists of a single peak in the disc overlap region,

[2] The ATCA is part of the Australia Telescope which is funded by the Commonwealth of Australia for operation as a national facility managed by CSIRO.

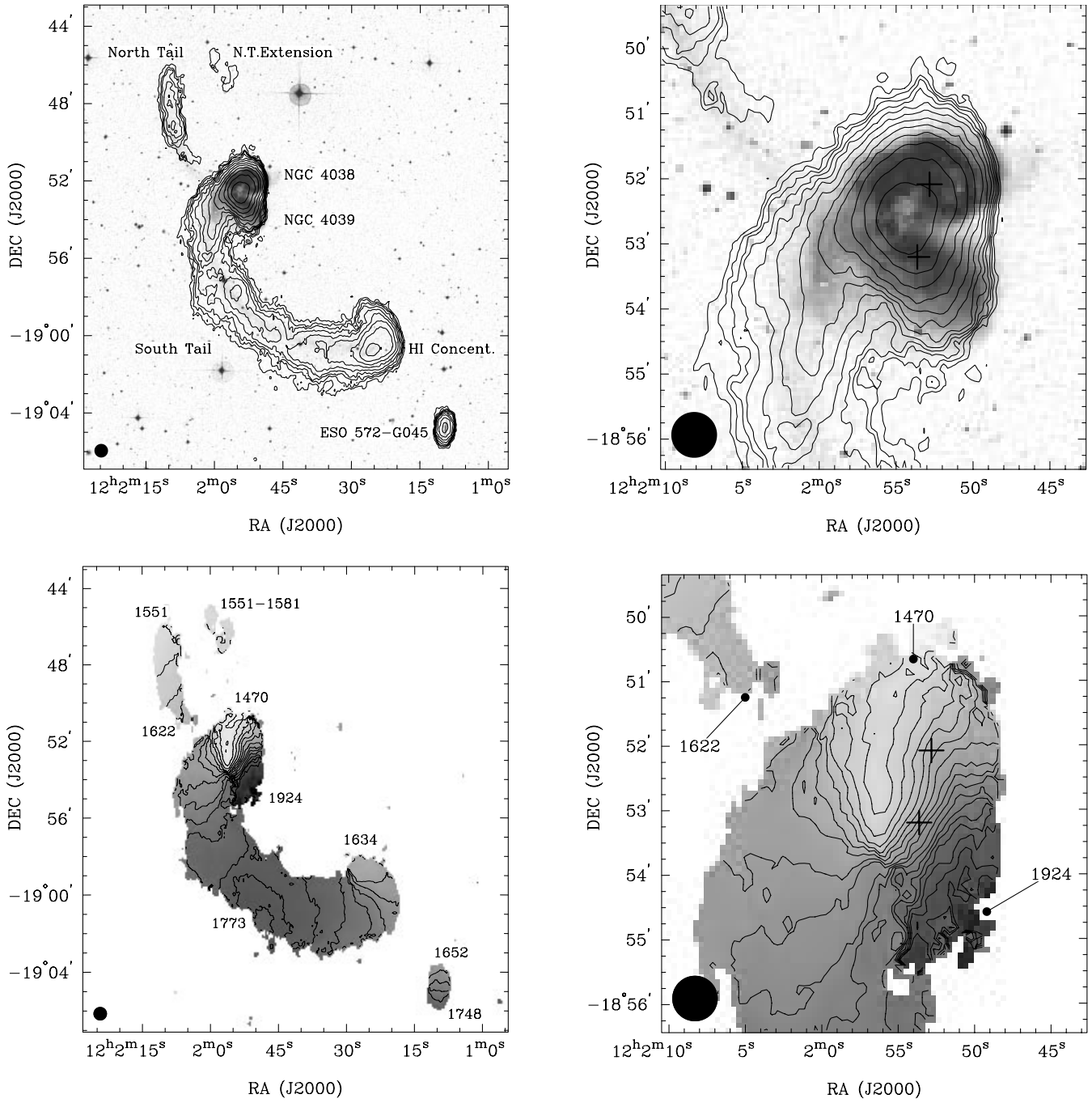

Figure 2. H I moment maps: those to the right are close-ups, enlarged by a factor of ∼ 3, and with crosses marking the galactic nuclei (Stanford et al. 1990). (a) and (b) The H I distribution (moment-0 in contours) overlaid on the optical image (see Fig. 1). Contours: 60, 120, 170, 240, 340, 480, 680, 960, 1360, 1920, 2715, 3840, 5430 Jy beam^{-1} m s^{-1}, i.e. powers of $2^{1/2}$. This is also $\sim 6.66 \times 10^{22} \times 2^{n/2}$ cm^{-2} ($n \geq 0$). (c) and (d) The H I mean velocity field (moment-1). Contours: 1520–1780 km s^{-1}, in steps of 20 km s^{-1}, plus 1800, 1820, and 1840 km s^{-1} in the close-up. (e) and (f) The H I velocity dispersion (moment-2). Contours: 15, 20, 25, and 30–140 km s^{-1}, in steps of 10 km s^{-1}. Labels indicate individual components as well as velocity peaks and ranges. The restoring beam (42 arcsec) is shown at the bottom left corner.

generally brightening with increasing velocity. Above 1560 km s^{-1} a second peak to the south is seen, moving southward and forming the inner half of the southern tail. A third peak beginning at ∼1610 km s^{-1} forms the outer half of that tail, the two meeting near the centre of the tail and disappearing at ∼1780 km s^{-1}. The northern tail is also detected (∼1540–1620 km s^{-1}) and possesses a previously unknown extension towards the west at a similar velocity.

The dwarf galaxy ESO 572–G045, about 30 kpc south-west of the tip of the southern tail, is detected in the velocity range of ∼1650–1750 km s^{-1}.

3.2 H I statistics

The disc region and the southern tail have similar H I masses of $\sim 2.3 \times 10^9$ and $\sim 2.5 \times 10^9$ M$_\odot$, respectively (see Table 3). The

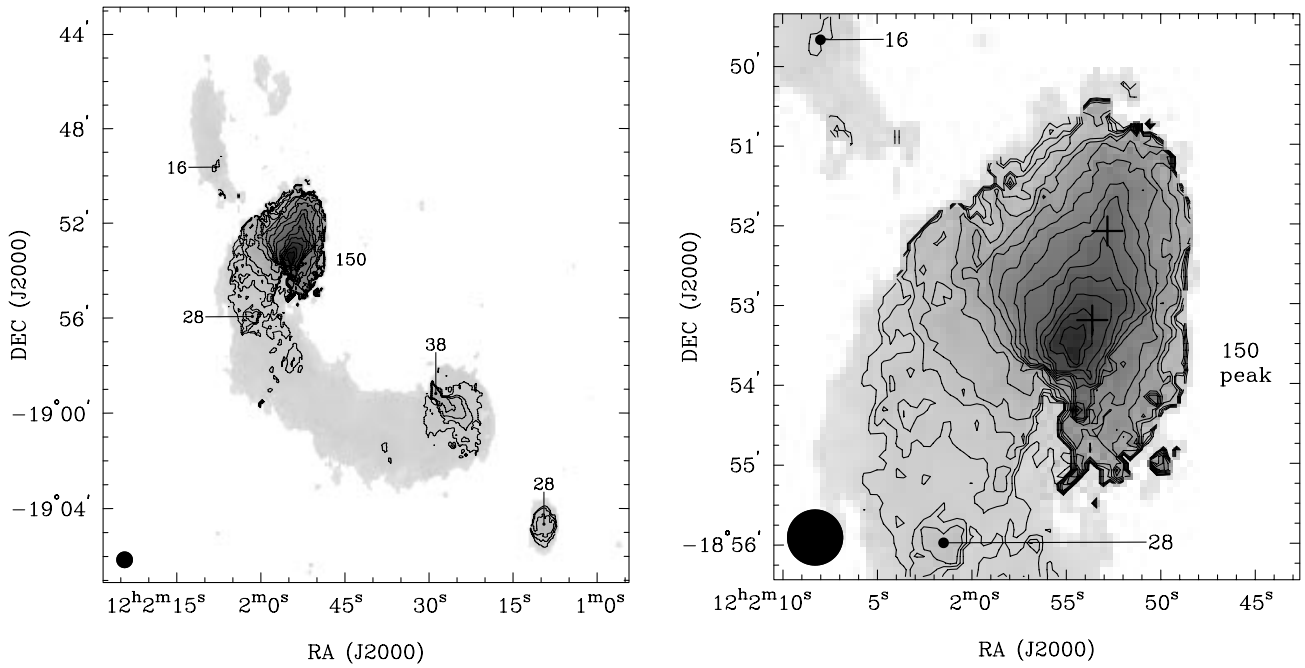

Figure 2. – *continued*

Table 3. H I flux statistics for various regions of the Antennae group, following primary-beam correction. The H I velocity ranges are estimated from the channel maps (see Fig. 8, later). Mass percentages are relative to the combined mass of NGC 4038/9 and ESO 572–G045.

Region	H I velocities ($km\,s^{-1}$)	H I flux ($Jy\,km\,s^{-1}$)	H I mass ($M_\odot$)	Fraction of total	Peak integrated intensity ($Jy\,beam^{-1}\,km\,s^{-1}$ and $\times^{20}\,cm^{-2}$)	J2000 peak position RA (± 2.5 arcsec)	Dec (± 2.5 arcsec)
Galactic discs	1340–1945	26.3	2.28×10^9	45%	5.62; 35.0	$12^h01^m54^s$	−18°52′40″
Southern tail	1590–1784	28.8	2.50×10^9	49%	1.59; 9.9	$12^h01^m25^s$	−19°00′44″
– tip only	1634–1740	10.5	8.23×10^8	18.0%	1.59; 9.9	$12^h01^m25^s$	−19°00′44″
Northern tail		2.05	1.78×10^8	3.5%	0.37; 2.3	$12^h02^m09^s$	−18°49′13″
– main section	1550–1622	1.84	1.60×10^8	3.1%	0.37; 2.3	$12^h02^m09^s$	−18°49′13″
– extension	1550–1580	0.21	1.81×10^7	0.25%	0.15; 0.93	$12^h01^m57^s$	−18°46′08″
ESO 572–G045	1640–1750	1.61	1.40×10^8	2.7%	1.10; 6.9	$12^h01^m09^s$	−19°04′41″
			Combined totals:				
Both tails		30.9	2.67×10^9	53%	1.59; 9.9	$12^h01^m25^s$	−19°00′44″
Southern tail + discs		54.9	4.77×10^9	94%	5.62; 35.0	$12^h01^m54^s$	−18°52′40″
Both tails + discs		56.9	4.95×10^9	97%	5.62; 35.0	$12^h01^m54^s$	−18°52′40″
The whole system		58.6	5.08×10^9	100%	5.62; 35.0	$12^h01^m54^s$	−18°52′40″

exact division between the two regions is arbitrary since there is no clear boundary between them, although the southern tail only has velocities above $\sim$1590 $km\,s^{-1}$. The northern tail has an H I mass of $\sim0.2\times10^9\,M_\odot$.

We calculate an H I mean velocity for the Antennae, of $\sim$1664 $km\,s^{-1}$, obtained from the moment maps (Figs 2a and b; the mean for the discs is $\sim$1620 $km\,s^{-1}$). This is similar to the $\sim$1660 $km\,s^{-1}$ systemic velocity obtained from optical measurements of the nuclear velocities (see Table 1).

The column density in Table 3 is obtained from the H I moment-0 map using the following formula:

$$N_{\rm HI} = 1.11\times10^{24}\,{\rm cm^{-2}}\,\frac{\int B(v)\,{\rm d}v}{{\rm Jy\,beam^{-1}\,km\,s^{-1}}}\,\frac{\rm arcsec^2}{\theta_1\theta_2}, \quad (1)$$

where $B(v)$ is the surface brightness, v is the velocity, and θ_1 and θ_2 are the major and minor beam full width at half-maximum (FWHM). For our H I maps with a resolution of 42 arcsec there is $6.23\times10^{20}\,cm^{-2}$ per $Jy\,beam^{-1}\,km\,s^{-1}$ of moment-0.

The H I mass is calculated from the integrated H I flux, $F(v)$, using the following equation (Roberts 1975; Giovanelli & Haynes 1988):

$$M_{\rm HI} = 2.356\times10^5\,M_\odot\left(\frac{D}{\rm Mpc}\right)^2\frac{\int F(v)\,{\rm d}v}{\rm Jy\,km\,s^{-1}}. \quad (2)$$

For $D = 19.2$ Mpc this gives $8.68\times10^7\,M_\odot$ per $Jy\,km\,s^{-1}$ of H I flux.

3.3 The galactic discs

The overall shape of H I in the disc region and at the base of the southern tail (Fig. 2b) follows the shape of the optical emission, except that: (1) the H I spans the gap between the western ends of

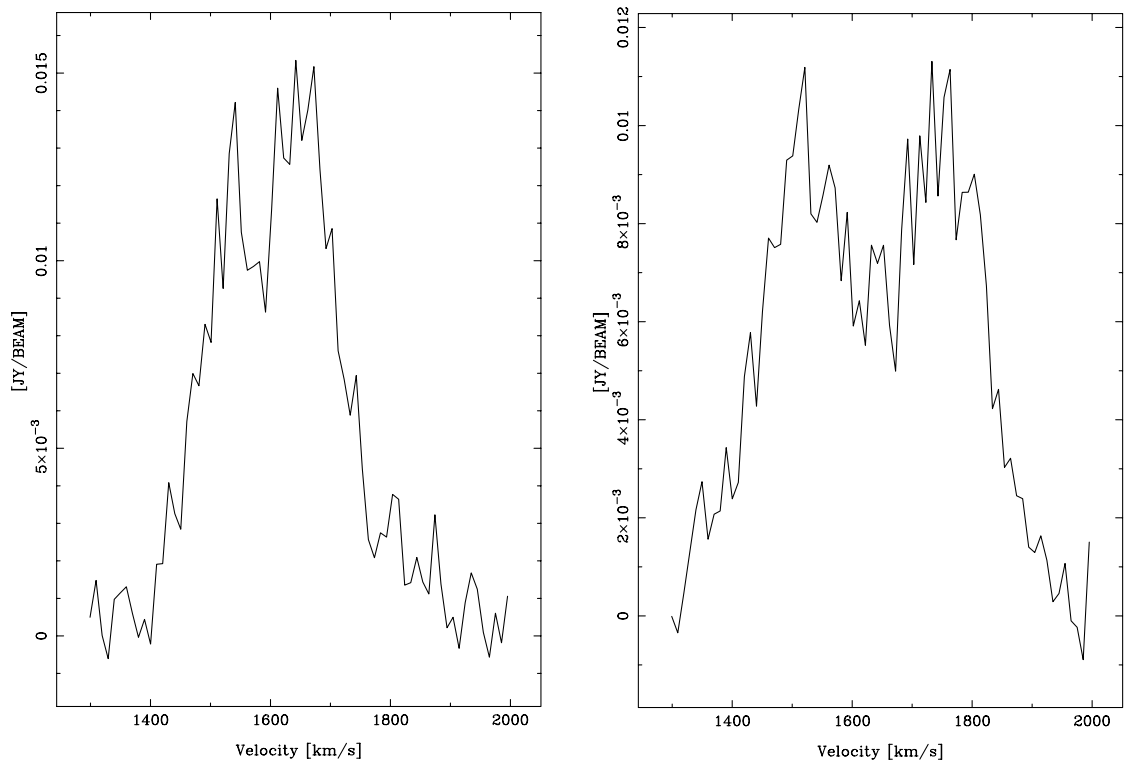

Figure 3. H I spectra at the positions of the two nuclei: (a) NGC 4038 (northern nucleus) and (b) NGC 4039 (southern nucleus); see Table 1). Both spectra show two emission peaks. Conversion: 1 Jy beam^{-1} $\approx 6.23 \times 10^{20}$ cm^{-2} (km s^{-1})$^{-1}$ $\approx$ 342 K.

the two discs and ends well inside the optical image, particularly in the northern disc, whereas galaxies usually have more extended H I; (2) the northern (and smaller) tidal tail is not connected to the discs in H I, with a ∼1-arcmin gap in the H I distribution; and (3) the H I intensity peak is midway between the optical nuclei.

The peak in the H I distribution lies at about one third of the distance between the two nuclei, about 32 arcsec (3 kpc) north of the centre of NGC 4039 (Table 3).

H I spectra taken throughout the discs generally show a single peak in the spectrum. However, there are two velocity peaks in a wide region midway between the centres of the two discs (Fig. 3), at ∼1542 and ∼1630 km s^{-1}. These peaks are also visible in the overall disc spectrum (Fig. 4a), but they do not match the systemic velocities of the discs which are ∼1663 and ∼1655 km s^{-1} (Table 1).

The velocities in the discs (Figs 2c and d) range from 1470 km s^{-1} at the northern disc edge, to 1920 km s^{-1} close to the south-western disc edge.

The discs have a substantial H I velocity dispersion (see Fig. 2f), with a peak of ∼150 km s^{-1} about 30 arcsec south of the NGC 4039 nucleus (Table 1), far from the intensity peak. The high dispersion results from the dual-peaked spectrum in its vicinity.

The dominant feature in the south-east is the base of the southern tail, which attaches smoothly to the discs. Although a clear division is seen in the *pv* diagram (Fig. 5a) the two are not clearly divided in the moment maps. Slices through the H I cube, taken along the major axes of NGC 4038 and 4039 (Fig. 6) show a velocity gradient, but do not permit calculation of a rotation curve.

3.4 The southern tail

The southern tidal tail describes a gradual but pronounced arc, about 90 kpc long, which dominates the maps (Fig. 2). It contains ∼14 times more H I than the northern tail, even though the two appear similar optically. It appears continuous, although some clumping is visible in Fig. 2a.

The optical width of the tail is quite narrow compared to H I. Gaussian fits to H I profiles across the tail give FWHM ≈ 100 arcsec.

The H I flux peaks at ∼1.59 Jy beam^{-1} km s^{-1} (9.9×10^{20} cm^{-2}) close to the tip of the tail. This is quite a pronounced concentration containing an H I mass of $\sim 8.2 \times 10^8$ M$_\odot$ or ∼30 per cent of the total for the tail, and was known as a distinct H I region in the maps by van der Hulst (1979).

The southern H I tail covers a continuous velocity range of ∼1590–1784 km s^{-1}, with the velocity changing smoothly along the tail, peaking at ∼1773 km s^{-1}. Towards the apparent concentration at the tip of the tail, the velocity changes rapidly towards a minimum of ∼1634 km s^{-1}. The iso-velocity contours change orientation suggesting that the tail bends sharply towards the end, in agreement with a sharp bend in the optical image. Hence this concentration might be just the result of projection in a tail with varying orientation.

3.5 The northern tail and extension

Compared to the southern tail, the northern tail contains less H I (∼1.6×10^8 M$_\odot$), is shorter and covers a smaller radial velocity range (1550–1620 km s^{-1}). Its velocity decreases steadily with distance from the discs.

There is a notable H I gap between the northern tail and the discs (see Figs 2b and 8). However, the *pv* diagrams (Fig. 5) suggest that a faint connection may exist. This gap contrasts with the optical

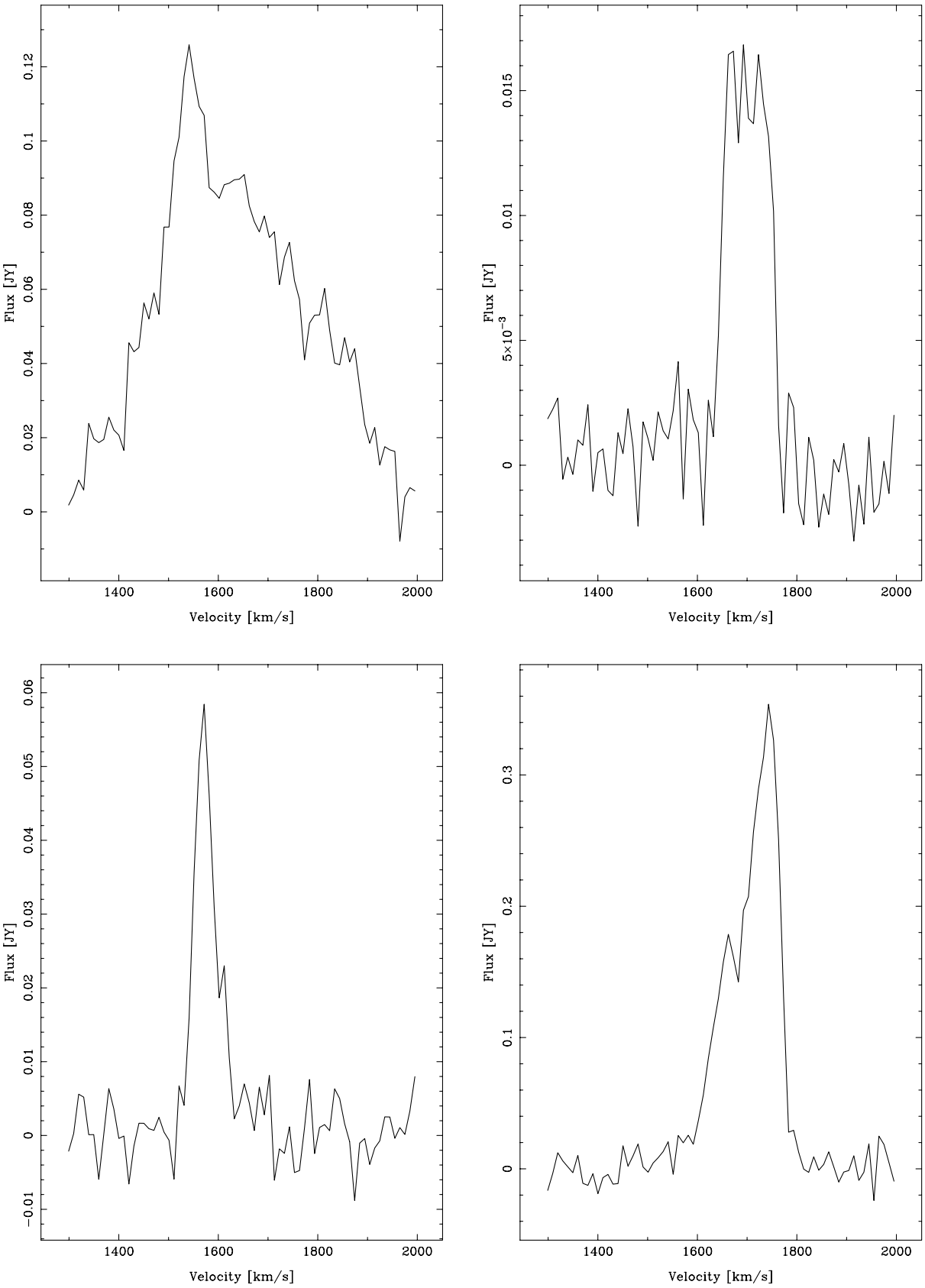

Figure 4. H I spectra of various regions in the Antennae group, integrated spatially. Conversion: $1\,\mathrm{Jy} \approx 8.68 \times 10^7\,\mathrm{M}_\odot\,(\mathrm{km\,s^{-1}})^{-1}$. (a) The Antennae discs; (b) ESO 572–G045; (c) the northern tail; (d) the southern tail.

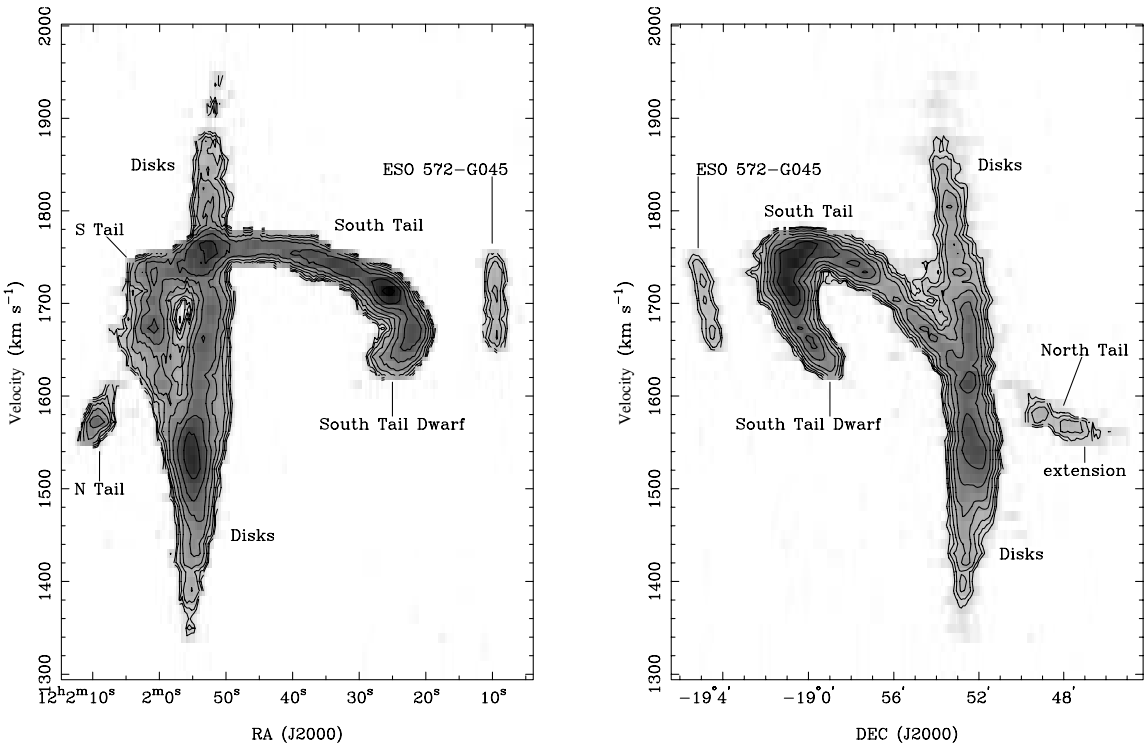

Figure 5. H I position–velocity (*pv*) diagrams, obtained by integrating the channel maps along a spatial axis, after clipping to exclude noise: (a) integrated along the Dec axis, (b) integrated along the RA axis. Contours (both cases): 0.2, 0.282, 0.4, 0.565, 0.8, 1.12, 1.6, 2.3, 3.2, 4.5, 6.4 Jy beam^{-1} arcsec, i.e. powers of $\sqrt{2}$. Conversion: 1 Jy beam^{-1} arcsec $\approx 4.62 \times 10^5$ M$_\odot$ (km s^{-1} kpc).

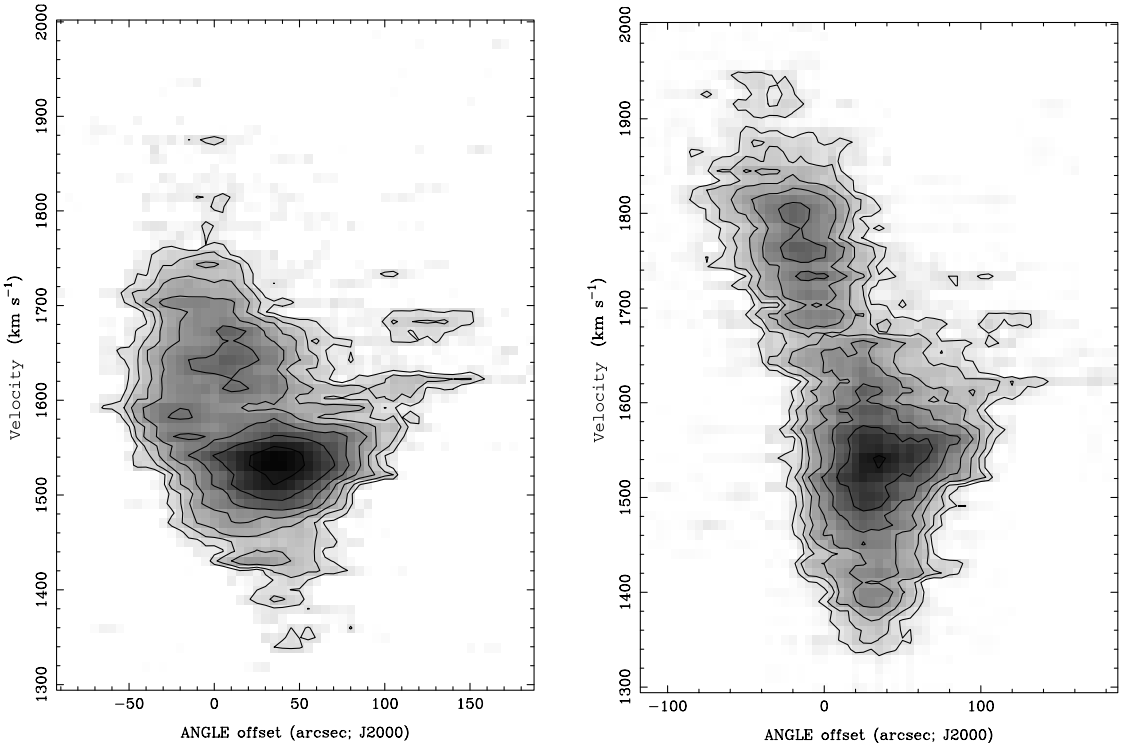

Figure 6. H I *pv* slices, obtained by sampling the channel maps along lines through the nuclei of each galaxy, roughly along their optical major axes. East is to the left, west to the right: (a) for the northern disc (NGC 4038), PA $\approx 98\overset{\circ}{.}7$, (b) for the southern disc (NGC 4039), PA $\approx 56\overset{\circ}{.}5$. Contours: $3\sigma \times 2^{n/2} \approx 2.7, 3.82, 5.4, 7.64, 10.8, 15.3, 21.6 \times 10^{-3}$ Jy beam^{-1} ($n \geq 0$).

connection of the tail to the discs and the continuous H I in the southern tail.

Fig. 2a shows the H I emission slightly west of the tip of the northern tail, not corresponding to any optical feature and not noted in any of the previously published H I maps. It has an H I mass of $\sim 1.8 \times 10^7\,M_\odot$ and a velocity range of 1550–1580 km s^{-1}. Its closeness to the tip of the northern tail suggests that this is a westward extension of a curved northern tail.

3.6 The dwarf companion ESO 572–G045

Our H I maps (see Figs 2a and b) show a clear H I detection of the small edge-on spiral galaxy ESO 572–G045 (Karachentsev, Karachentseva & Paranovskij 1993; see also Table 1). Optically it has a size of $\sim 64 \times 7$ arcsec^2. It is $\sim$16.5 arcmin (91 kpc) from the centre of the Antennae, and $\sim$5–6 arcmin south-west of the end of the southern tail.

In H I the galaxy is slightly extended north–south, but unresolved east–west, matching the optical appearance quite well. It has a clear and smooth velocity gradient along the north–south major axis, ranging from 1650–1750 km s^{-1} (north to south), like an edge-on view of a rotating disc. Its velocity also matches the adjacent portions of the Antennae southern tail. There is no visible bridge of material joining this galaxy to the tidal tail, and also no visible distortion of the tail in the direction of this galaxy.

The H I mass of ESO 572–G045 is $\sim 1.4 \times 10^8\,M_\odot$, or 3 per cent of that in the Antennae. Its systemic velocity is $\sim$1700 km s^{-1}.

3.7 Radio continuum emission

The ATCA 20-cm continuum map (Fig. 7a) corresponds to those published by Condon (1983, 1987), and by Hummel & van der Hulst (1986), all using the VLA data. However, the 13-cm map obtained with the ATCA (Fig. 7b) is the first ever published.

The continuum sources seen in and around the Antennae are summarized in Table 4. The images show no emission outside the vicinity of the galactic discs, except for a number of point sources. No continuum emission from the dwarf galaxies was detected.

Fig. 7 shows the continuum concentrated in the northern starburst ring and in the disc overlap region, with some additional extended emission. The emission is well correlated with the location of star formation activity as seen through optical, Hα and infrared mapping (Amram et al. 1992; Mirabel et al. 1998; Whitmore et al. 1999, respectively). The continuum appears generally more extended than these regions.

The major peak in the radio continuum at both 20 and 13 cm occurs in the disc overlap, with secondary peaks near the southern nucleus and in the western portion of the starburst ring, as for the mid-infrared (Mirabel et al. 1998). Sources A, B, and C correspond to the three molecular gas concentrations found in CO by Stanford et al. (1990).

Source A, in the overlap region, is particularly bright. It corresponds to 'Region C' of Whitmore & Schweizer (1995), and to the 'East Clump' of Stanford et al. (1990). Higher resolution 13-cm maps (not shown), with a fitted Gaussian restoring beam rather than the larger circular one of Fig. 7, show this region resolved into three or four smaller ones, apparently corresponding to the southern-most group of emission regions seen in Hα by Amram et al. (1992).

Source B is at the catalogued central or at the nuclear position of NGC 4038 (Table 1), while source C is $\sim$6 arcsec west of the nucleus of NGC 4039.

The 20-cm map has slightly lower resolution than the 13-cm map (see Fig. 7) and shows more extended emission, seen largely as a number of faint 'protrusions' from the Antennae discs, some of which are noise. Because of the higher resolution, the 13-cm map resolves more emission peaks, particularly in the southern disc, and shows two depressions which are not obvious at 20 cm.

Fig. 7 also shows some continuum emission coming from the base of the southern tail, which is rather bright optically and in H I (Fig. 2b). There is no trace of radio continuum emission elsewhere in either tail.

We measure the total continuum emission from the discs as $\sim$498 mJy at 1413 MHz (20 cm), and $\sim$311 mJy at 2378 MHz (13 cm). This includes the emission at the base of the southern tail. The 20-cm figure compares with the 472 ± 23 mJy at 1465 MHz by Condon (1983), 572 mJy at 1490 MHz by Condon (1987), and 486 ± 20 mJy at 1465 MHz by Hummel & van der Hulst (1986).

4 DISCUSSION

4.1 H I mass distribution

The total H I mass of the Antennae, as measured with the ATCA, is $\sim 5 \times 10^9\,M_\odot$. About 46 per cent of the H I mass is in the discs, 51 per cent in the southern tail and only 3 per cent in the northern tail (see Table 3). Van der Hulst (1979) estimated the corresponding components as 40, 52 and 8 per cent. The column densities in the discs are much higher than those in the tails. Our measurements agree with the general trends found previously (e.g. Hibbard & van Gorkom 1996), whereby gas is depleted in the galactic discs as their merger progresses, leaving most of it in the tidal tails. For the Antennae, at an early stage of merging, the tails already contain about half of the H I.

The southern tail is about twice as long optically as the northern tail, but otherwise they are optically similar. In H I this is quite different, with the southern tail containing $\sim$15 times as much H I as the northern tail. Additionally, the northern tail is not connected to the discs in H I.

Wilson et al. (2000) mapped the molecular gas in the discs and found that about half of the detected gas resides in five super-giant molecular cloud complexes in the disc overlap. The remainder is in the galactic nuclei and the western portion of the northern star-forming ring. However, the authors acknowledge, based on single-dish observations by Gao et al. (1998), that they probably missed 60 per cent of the gas. More recently, Gao et al. (2001) gave a molecular mass estimate of $\sim 1.38 \times 10^{10}\,M_\odot$ (adopting $D = 19.2$ Mpc). Combined with our H I data, this implies a molecular-to-H I mass ratio of $\sim$6:1 for the discs alone and $\sim$3:1 for the whole Antennae.

Gao et al. (2001) made the first, tentative detection of CO at the tip of the southern tail, with a molecular mass of $\sim 2 \times 10^8\,M_\odot$, and hence a molecular-to-H I ratio of $\sim$1:4.

Van der Hulst (1979) tried to overcome the large angular size of the Antennae, and Westerborks low sensitivity to the east–west structure, by estimating H I masses from multiple single-disc measurements by Huchtmeier & Bohnenstengel (1975). The derived total H I mass is $3.7 \times 10^9\,M_\odot$, much more than the $2.5 \times 10^9\,M_\odot$ which he measured by synthesis imaging, but less than our measured $\sim 5.1 \times 10^9\,M_\odot$ (including ESO 572–G045), and the estimate of $\sim 5.3 \times 10^9\,M_\odot$ by Huchtmeier & Bohnenstengel

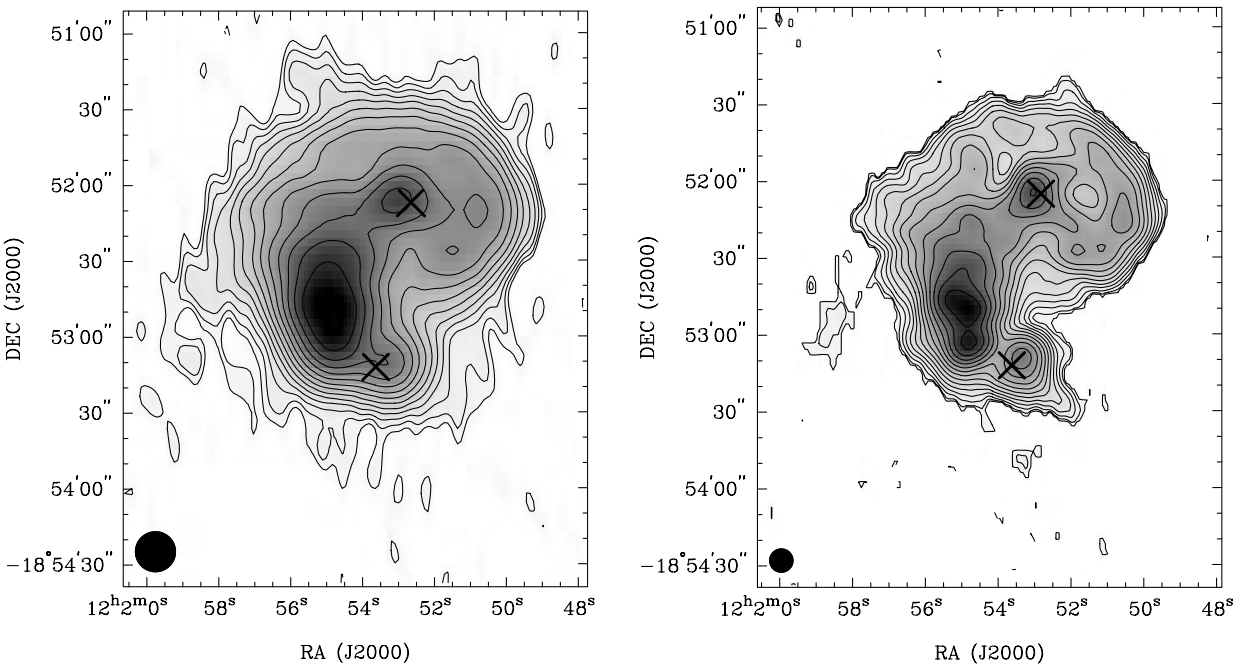

Figure 7. Displayed are the 20- (left) and 13-cm (right) radio continuum images of the Antennae. The beams, shown in the bottom left corner, are 16 and 9.5 arcsec, respectively, using 'uniform' weighting. (a) 20-cm map: rms noise: 2.4×10^{-4} Jy beam^{-1}; contours: −0.72, 0.72, 1.02, 1.44, 2.04, 2.88, 4.07, 5.76, 8.15, 11.5, 16.3, 23.0, 32.6, 46.1, 65.2 mJy beam^{-1}. 1 mJy beam^{-1} ≈ 0.39 mJy kpc^{-2}. (b) 13-cm map: rms noise: 6.1–6.5 × 10^{-5} Jy beam^{-1}; contours: −0.18, 0.18, 0.255, 0.360, 0.509, 0.720, 1.02, 1.44, 2.04, 2.88, 4.07, 5.76, 8.15, 11.5, 16.3 mJy beam^{-1}. 1 mJy beam^{-1} ≈ 1.12 mJy kpc^{-2}.

(1975). The component masses measured by van der Hulst (1979) were 1.0×10^9 M$_\odot$ for the discs, 1.3×10^9 M$_\odot$ for the southern tail, and 1.8×10^8 M$_\odot$ for the northern tail (adopting $D = 19.2$ Mpc).

4.2 The galactic discs

4.2.1 Disc H I

Both the H I distribution and the velocity pattern in the central area of the Antennae (Figs 2b and d) do not resemble the regular, symmetric pattern seen in an isolated disc or spiral galaxy, and there is also no clear way to model it as the superposition of two discs.

Our data suggests instead (i) that disc H I has been extensively kinematically disturbed by disc collision or the preceding close encounter, (ii) that it is now largely detached from the individual galaxies, with most of it no longer following closely their original disc structure, and (iii) that it resides largely in a single structure between and surrounding the discs. Further, this structure is connected smoothly to the H I-rich southern tidal arm.

Mihos & Hernquist (1994) ran computer simulations of a variety of merging disc galaxy pairs, including both those with and without large bulges. In the simulations, a clear pattern was seen. Galaxies with no bulge experienced nuclear gas inflows early in the merger, producing a steady moderate starburst and depleting the gas prior to the final stages of the merger. However, the presence of a substantial bulge inhibited this inflow, with a low initial star formation rate and minor gas depletion. The result for these systems was coalescence of the two galaxies' still abundant gas late in the merger, resulting in a massive burst of star formation and an ultraluminous infrared merger.

This study sheds light on the possible origin of the observed H I pool in the Antennae, and their future evolution. The star formation consequences of this are described further in Section 4.6.

Although there is an apparent pooling of the H I, the dual-peaked spectra, seen particularly over the central southern disc, indicate that in this region at least there are two clouds overlapping along the line of sight, with some of the H I still attached to the southern disc.

4.2.2 Disc radio continuum

Comparison of our ATCA 20- and 13-cm radio continuum data (Fig. 7) with VLA maps at 20 and 6 cm (Hummel & van der Hulst 1986) does not reveal many new features.

The 13-cm continuum map (beam = 9.5 arcsec) resembles a smoothed version of the high-resolution 6- and 20-cm VLA maps (beam = 6 arcsec). The latter resolve greater detail in the discs, e.g. more emission peaks in the eastern half. The faint emission at the base of the southern tail is not seen in these maps, but is clearly detected in the low-resolution VLA 20-cm map.

The low-resolution 20-cm map by Hummel & van der Hulst (1986) has the same sensitivity and resolution as our Fig. 7(a), allowing a direct comparison. The measured fluxes agree well within the errors. Our image includes slightly more extended emission at faint levels, but most of it is likely to be noise.

The well-resolved emission peaks in our radio continuum maps, particularly in the 13-cm image (Fig. 7b), agree with those in the Hα map by Amram et al. (1992). Our resolution is too low to allow a detailed comparison of the radio continuum and Hα peaks.

With radio continuum closely matching optical H II regions and Hα maps, the Antennae agree with the correlation between star formation and the Hα, FIR, and radio, noted for example by Sanders & Mirabel (1985).

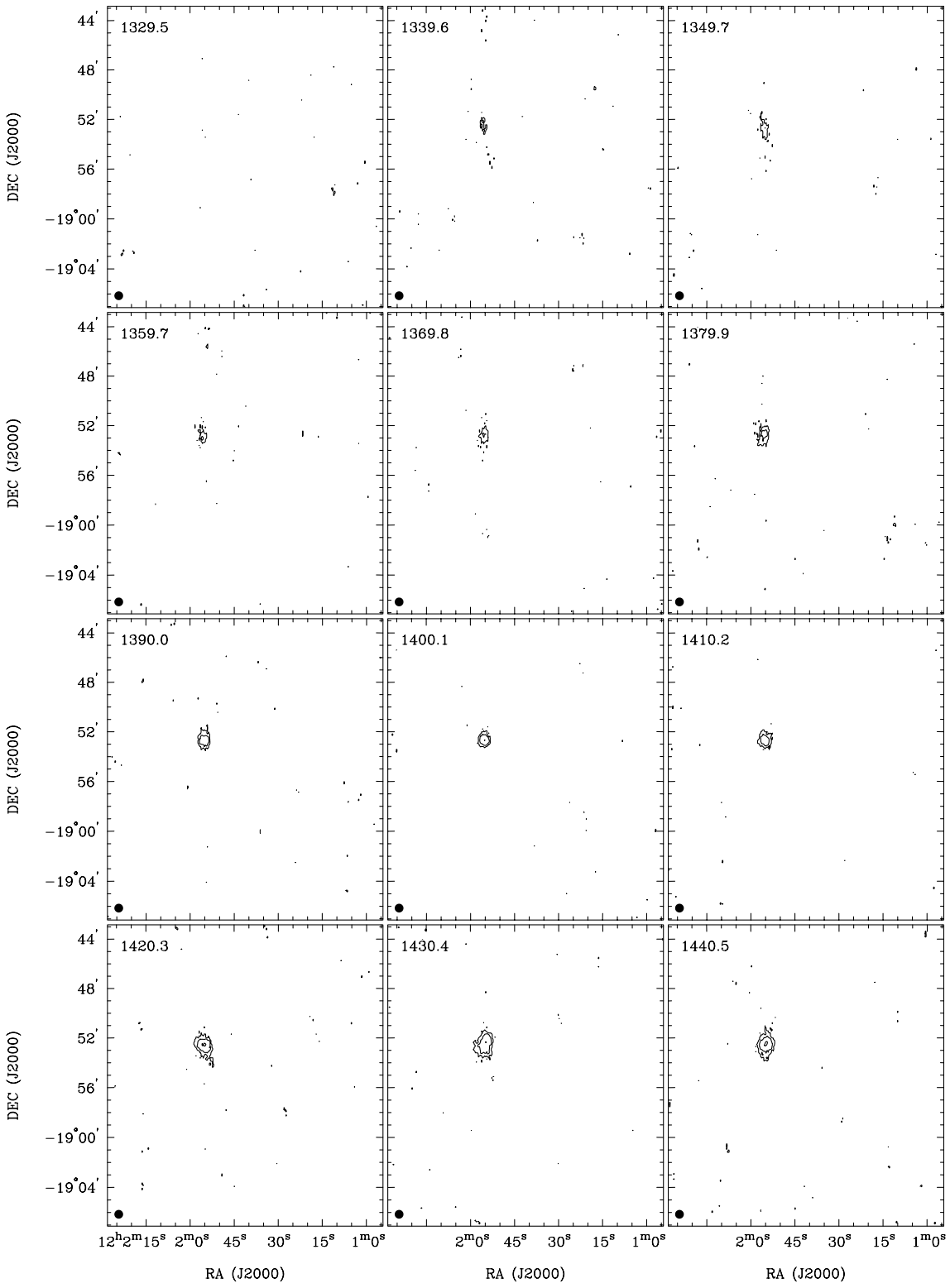

Figure 8. H I channel maps for the Antennae group. Contours: -3σ, $3\sigma \times 2^n = -2.7, 2.7, 5.4, 10.8, 21.6, 33.2, 66.4$ mJy beam^{-1}, or $\sim 1.7 \times 10^{18} \times 2^n$ cm^{-2} (km s^{-1})$^{-1}$ ($n \geq 0$). Also 1 Jy beam$^{-1} \approx 342$ K [from equation (12.2) in Giovanelli & Haynes 1988]. The 42 arcsec beam is shown at the bottom left.

4.3 The tidal tails

4.3.1 Modelling the tails

Toomre & Toomre (1972) performed pioneering computer simulations which clearly demonstrated for the first time that galactic tails originate through tidal interaction. However, these simulations entirely neglected the self-gravity of the disc material as well as dispersion effects, which have been considered in more recent simulations. The omission of simulated

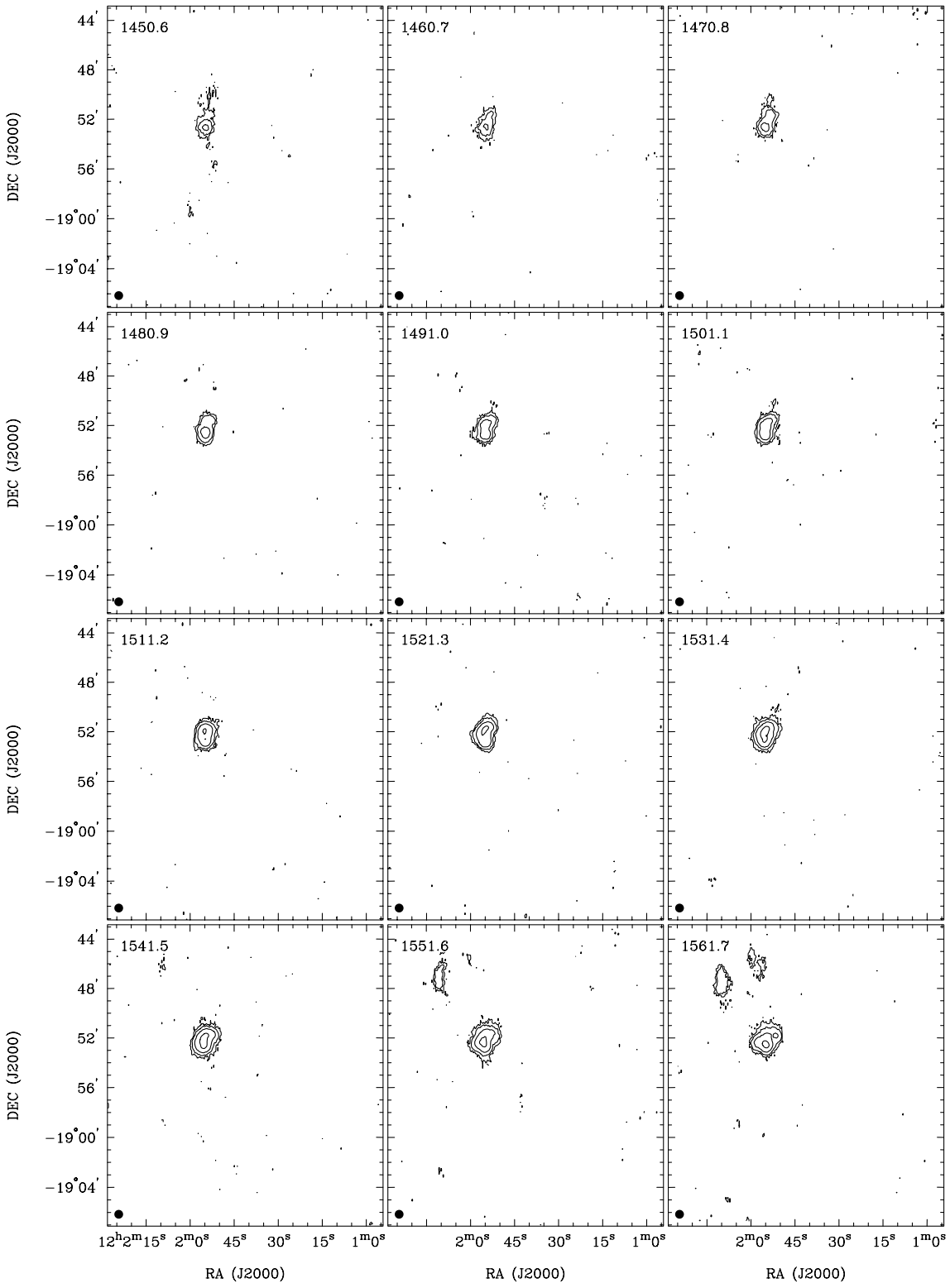

Figure 8. – *continued*

velocity fields in many theoretical papers on galaxy interactions often renders a direct kinematic comparison between H I observations and model predictions impossible.

Fortunately, van der Hulst (1979) obtained and published graphically the velocity information not published by Toomre & Toomre (1972), and used it to compare observed *pv* diagrams to predicted ones. After rescaling of dimensions to fit the data, the match was quite close.

Computer simulations (e.g. Appendix VIII of Hibbard 1995; Hibbard & Mihos 1995) predict that material in a tail will be ejected along many different trajectories, with a large-scale filament-like structure as a result of the similarity of trajectories

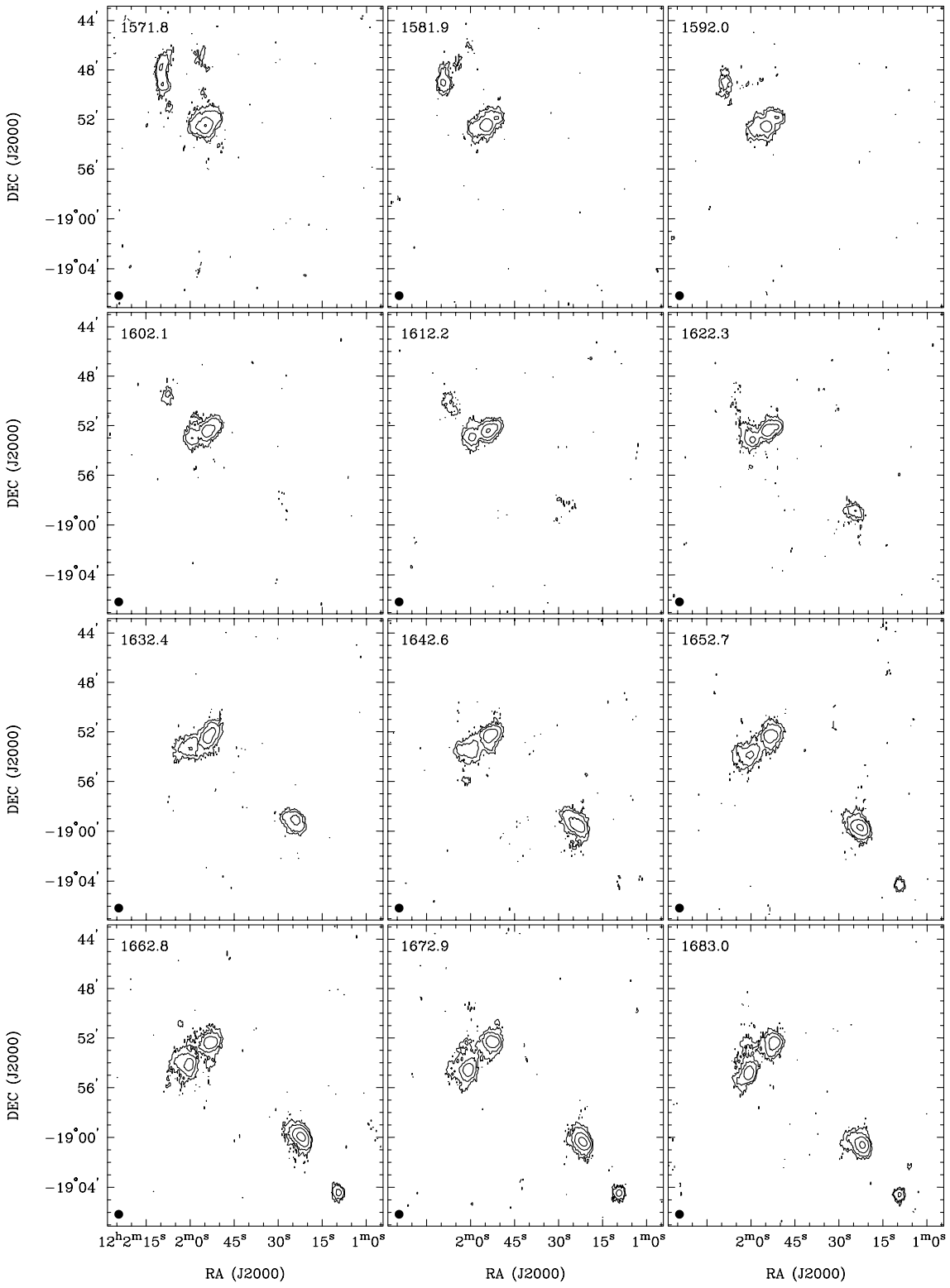

Figure 8. – *continued*

of neighbouring material, rather than being a stream of material along a common trajectory. In this way, it resembles a density wave, with the wave initially moving outward from the galactic discs, and in most cases later falling back inward under gravity. Consequently, the material velocities tend to be at a large angle to the orientation of the tail, and disc galaxy models do not apply to tidal tails.

More recently, Barnes (1988) carried out tree-code *N*-body simulations of interacting disc galaxies, incorporating full self-gravity and a bulge/disc/halo model. The first model made was a look-alike of the Antennae, for which a number of figures were published, including a *pv* diagram along the orbital plane, approximately north–south (see his fig. 3d). This is roughly a modelled equivalent of our Fig. 5(b), but showing all

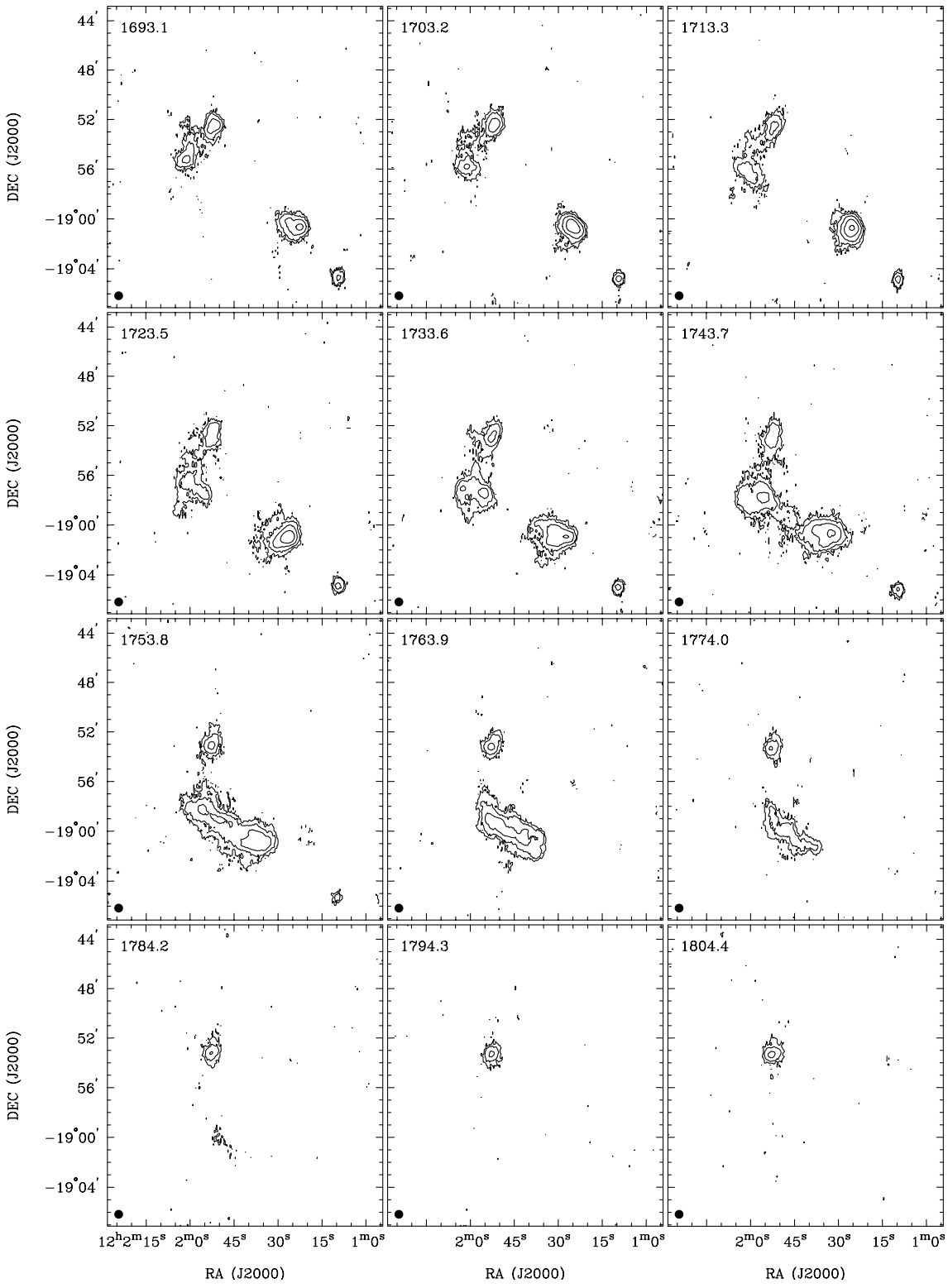

Figure 8. – *continued*

material originating from the disc rather than just H I. These two figures bear a very close resemblance, except that the observed southern H I tail is much more prominent than the northern one, whereas the model diagram shows them fairly comparable in size.

Hibbard & Mihos (1995) performed similar simulations based on earlier VLA H I data for the merging pair NGC 7252, which closely resembles the Antennae. The observed H I *pv* diagram (their fig. 1) closely resembles our observed ones for the Antennae (Fig. 5). That work particularly mentioned the final destination of material in tidal tails (their figs 5 and 7). The bulk of tail material has an elliptical trajectory taking it back towards the discs, much of it quite rapidly. Some material, however, may gain escape velocity. Material further from the centre of the disc also has higher velocities.

By analogy, it can be inferred that the outer-most material in the

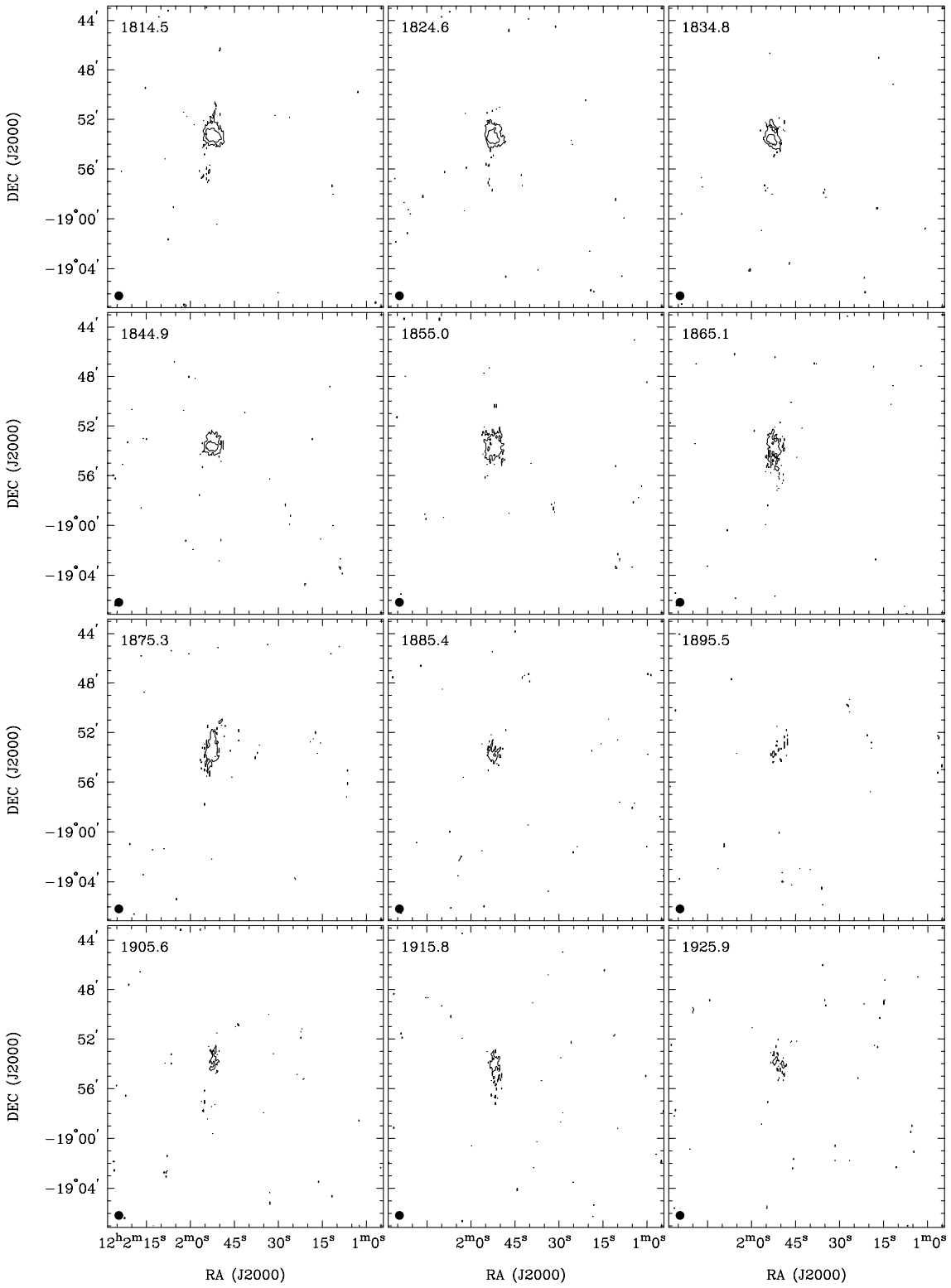

Figure 8. – *continued*

southern tail of the Antennae (including the concentration at the tip), may take some time to fall back, if it does at all. However, the turnaround in radial velocities in the southern tail indicates that it is substantially bent along the line of sight 'towards' the discs, suggesting that the tip is falling back. This interpretation, though, is unlikely to be correct since computer simulations show that the energy of the tail material increases with distance from the centre, and thus outer portions of the tail will take longer to fall back (Hibbard, private communication).

4.3.2 Optical versus H I emission in the tidal tails

There is no obvious spatial displacement between the optical and H I emission in the tails (Fig. 2) as has been observed in other

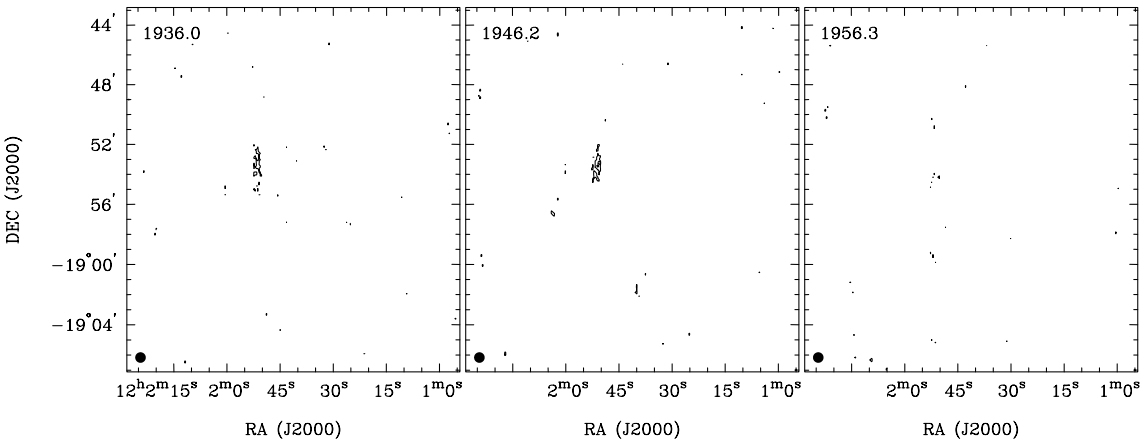

Figure 8. – *continued*

Table 4. A list of radio continuum sources (including previous identifications); sources A, B, C, and D are in the Antennae. The diffuse continuum emission from the galactic discs is discussed elsewhere.

Source name /Identifier	Peak position RA	DEC	Peak flux density (mJy beam^{-1}) 20 cm	13 cm	Comments
A	$12^h01^m55.0^s$	$-18°52'49''$	63.6	22	Overlap of discs (4 subregions)
B	$12^h01^m53.0^s$	$-18°52'06''$	32	10.5	NGC 4038 nucleus
C[(1)]	$12^h01^m53.3^s$	$-18°53'10''$	19[(1)]	6.5	5 arcsec south-east of NGC 4039 nucleus
D	$12^h01^m48^s$	$-18°55'15''$	1.6	1.6	Midway between dwarf galaxies
E	$12^h01^m45^s$	$-18°53'05''$	3.4	3.4	West of the galactic discs
F	$12^h01^m09.7^s$	$-18°43'39''$	11	<2	Extended ($\sim 100 \times 30$ arcsec^2) source (N–W)
TXS 1159-187	$12^h02^m12.3^s$	$-19°00'30''$	108	43	Catalogued radio source[(2)]
TXS 1158-187	$12^h01^m18.3^s$	$-19°02'19''$	78	36	Catalogued radio source[(2)]
MS 1200.2-1829	$12^h02^m52.6^s$	$-18°44'57''$	5		Known X-ray and optical source[(3)]

[(1)]This peak is poorly resolved because of contamination by neighbouring peaks, hence the value may not be accurate.
[(2)]Detected at 365 MHz by Douglas et al. (1996).
[(3)]$z = 1.83$, ~ 20 mag; see Gioia et al. (1990), Maccacaro et al. (1991) and Stocke et al. (1991).

interacting systems, e.g. Arp 157, Arp 220, and Arp 299 (see Hibbard, Vacca & Yun 2000). The primary differences are: (1) the widths of the tails, (2) the highly visible H I pool at the end of the southern tail, (3) the greater length of the southern tail in H I, and (4) the absence of H I at the base of the northern tail. The latter might be a result of ionization by emission from the discs as suggested by Hibbard, Vacca & Yun (2000).

The H I in the tails is clearly more extended laterally than the stellar emission. Short-exposure optical images (e.g. Fig. 1) show both the tidal tails to be fairly narrow with a width of 30–40 arcsec (2.8–3.7 kpc), much less than the H I width of $\sim$100 arcsec (9.3 kpc). Deeper optical images of the Antennae (Schweizer 1978), however, show both tails being more extended.

The strong stellar emission from the Antennae tails is unusual since most tidal tails are optically faint. This general trend may come about because material which is (pre-interaction) further from the galactic centre, is less tightly bound gravitationally, and more affected by intergalactic tidal forces, and thus generally contributes most of the material in tidal tails (e.g. Toomre & Toomre 1972). This and the fact that in most galaxies the gas is much more extended than the stellar component, leads to tails initially containing a lot of gas and relatively few stars. Furthermore, the rapid decrease in the gas density of tidal arms, because of differential expansion after their creation, should result in a corresponding decrease in star formation rates, and hence a drop in optical emission (Mihos, Richstone & Bothun 1991). The fact that the Antennae do not show low optical brightness, suggests that the material in the tails derives from a more inner part of the discs than what is often seen in other galaxies.

4.3.3 No continuum emission in the tidal tails

Although the discs show continuum emission, we have found none from either of the tidal tails, except at the base of the southern tail. Since radio continuum emission is generally produced extensively in star-forming regions, e.g. by hot gas or shocks in supernova remnants, its absence in the tails implies a low level of star formation.

The absence of detectable radio continuum in tidal tails is also quite common for other observed interacting systems, and agrees with predictions of Mihos et al. (1991) and others, who have undertaken computer simulations of interaction-induced starbursts, modelling galactic close encounters and the resulting collisions of giant molecular clouds and inwards gas flows, believed to be the means by which starbursts are produced in interacting galaxies. Mihos et al. (1991) studied star formation rates for pairs of disc galaxies undergoing encounters (but not mergers) at a number of separations and relative orientations. They found that in some cases

close encounters will actually reduce star formation, by throwing clouds out of the disc and reducing their density, without producing many collisions. However, prograde encounters (both discs rotating in the same sense as their orbit about one another, e.g. the Antennae), tend to produce strong starbursts and extensive transfer of material between discs. Such encounters could also produce starbursts along the leading edges of tidal tails. However, such tails expand rapidly and the star formation rate drops considerably after a couple $\times 10^8$ yr (Mihos et al. 1991), so that tails will generally have no detectable star formation activity when observed well into a close encounter or merger.

4.4 Southern-tail tidal dwarf galaxy

The enhanced H I column density at the tip of the southern tail coincides with the location of a young ($\sim 3 \times 10^8$ yr) star-forming region, suspected to be a dwarf galaxy formed during the interaction (Schweizer 1978; Mirabel et al. 1992). The enhancement, by a factor of ~4.5:1 compared to the minimum of the tail can at least in part be explained as a projection effect as a result of the bending of the tail and hence a deeper line of sight. However, such a large ratio requires a substantial bending angle, hence there is likely to be an enhanced local gas density at the location of the star-forming region: a point already made by van der Hulst (1979).

Sizeable concentrations in tidal arms, many of which appear self-gravitating, have been found in H I studies of a number of interacting galaxies, with typical H I masses of $\sim 5 \times 10^8$–6×10^9 $M_\odot$, the resulting overall population of bound dwarf galaxies being perhaps half of all dwarfs (Sanders & Mirabel 1996).

The formation of dwarf galaxies is predicted by computer simulations of galaxy interaction, such as those by Barnes & Hernquist (1992), and the more complete model, including gas dynamics, by Barnes & Hernquist (1996). In models, self-gravitation of some material ejected in tidal arms, may be enough to overcome expansion of the arm over time, forming bound objects. These tend to be gas-rich since their gas and stars have slightly different origins, with the gas being more compact and so surviving tidal disruption. Frequently a number of bound objects are produced, generally in the outer parts of the tail, because of the lower mass needed to avoid disruption there.

Elmegreen, Kaufman & Thomasson (1993) used computer models of IC 2163/NGC 2207 to show that extended discs of gas can lead to a massive concentration of gas at the end of a tidal arm during interaction. They also showed that if the mass of the second galaxy is similar to, or larger than, the host galaxy, then eventually massive clouds can be ejected from the host galaxy, leading to self-gravitating dwarf galaxies like those observed by the same authors using VLA H I observations. According to Elmegreen et al., the lack of an extended gas distribution in the models of Barnes & Hernquist (1992), prevented the gas pool forming in their simulations. With the Antennae galaxies merging, and of apparently similar masses, they should be sufficient to produce a pool along a tail, or attached or detached dwarf galaxies.

4.5 The dwarf companion ESO 572–G045

The galaxy ESO 572–G045 is much smaller and less massive than the Antennae and is classified as a spiral dwarf galaxy. It has an H I radial velocity of $\sim 1688\,\mathrm{km\,s^{-1}}$, similar to that of the southern tidal tail, and a small apparent distance from it.

The association between ESO 572–G045 and the Antennae could be found by searching it for signs of recent interaction (e.g. starburst activity). If this has not occurred then almost certainly the dwarf is not involved in the Antennae merger. If interaction has occurred, then either the dwarf was a pre-existing galaxy now tidally disturbed, or it is a bound object produced from the tidal debris of the merger (e.g. Hernquist 1992; Elmegreen et al. 1993; Barnes & Hernquist 1996). Given its apparent spiral structure, creation from debris appears a less likely explanation. With an H I mass alone of $\sim 1.4 \times 10^8$ $M_\odot$, its mass would be at the high end for bound objects (Barnes & Hernquist 1992), but still reasonable. Unfortunately, to date there is no available information to resolve this question.

The small size of the object relative to the beam allows only an approximate dynamical mass estimate from H I velocities. It is edge-on, hence its maximum rotational velocity is half of the H I range ($\sim 50\,\mathrm{km\,s^{-1}}$). The corresponding radius appears to be ~32 arcsec (3 kpc). The following equation (Giovanelli & Haynes 1988) estimates the total enclosed mass, assuming a spherical distribution:

$$M_T(r) = \frac{rV^2(r)}{\mathrm{kpc(km\,s^{-1})^2}} \times 2.33 \times 10^5\ M_\odot, \tag{3}$$

from which we derive a dynamical mass of $\sim 1.74 \times 10^9$ $M_\odot$. These estimates imply that H I makes up about 8 per cent of the mass of the dwarf, roughly in the range observed in larger spiral galaxies, and supporting the suggestion of a spiral structure.

The inner-most distance from the centre of a globular cluster or orbiting satellite, at which tidal stripping occurs, is the tidal radius (r_t), which we take as the Jacobi limit:

$$r_t = R\left(\frac{M}{3M_g}\right)^{1/3}, \tag{4}$$

where M is the total mass of the satellite, M_g that of the parent galaxy and R their separation (see e.g. Pisano & Wilcots 2000). Taking the velocity minima and maxima as the extreme velocities in the Antennae discs, and the H I peak as the centre of mass, leads to a projected rotation velocity of $\sim 228\,\mathrm{km\,s^{-1}}$ at a radius of ~12.5 kpc, and a very rough Antennae disc mass estimate of $\sim 1.5 \times 10^{11}$ $M_\odot$. Treating ESO 572–G045 as a satellite of the Antennae discs ($R \geq 91$ kpc) gives a tidal radius of $r_t \geq 14$ kpc, much larger than its measured H I radius. So it is unlikely that ESO 572–G045 is prone to disruption.

4.6 Star formation patterns

The Antennae starburst is optically spectacular and has a total infrared luminosity of $\sim 10^{11}$ $L_\odot$ indicating major starburst activity. However, Gao et al. (2001) concluded that the starburst is modest considering the high molecular gas content of the system (1.38×10^{10} $M_\odot$).

Computer models of the Antennae have shown that it may result from the prograde encounter of two disc galaxies. This has been found (e.g. for the non-merging case, by Mihos et al. 1991) to generally produce the strongest starburst. In the same study, closer encounters also strengthen the starburst at least for non-mergers. The Antennae encounter and the starburst within it thus agrees with the available models.

Mihos & Hernquist (1994) modelled star formation patterns in merging pairs of disc galaxies, concluding that galaxies with large bulges would delay their major starburst activity until the final stages of merger. At this point a combined central gas pool would

produce vigorous starbursts (and a high infrared luminosity). From our H I studies it appears that such a pool of cool gas is forming in the Antennae.

These observations suggest that the Antennae are an example of the delayed action for bulge galaxies modelled by Mihos & Hernquist (1994), with the current starburst being an early stage, and that the scene is being set for a fairly spectacular final merger of the discs at a later date.

5 CONCLUSION

Our H I images of the Antennae have higher sensitivity and resolution than those of van der Hulst (1979), revealing more H I mass and structure as well as some new features not observed previously.

Our radio continuum images include the first published 13-cm image, and a new 20-cm image corresponding to previously published ones by Condon (1983, 1987) and Hummel & van der Hulst (1986). No continuum polarization has been detected. The radio continuum maps closely resemble the Hα maps of Amram et al. (1992). The distribution approximates the optical star-forming regions, e.g. seen in *HST* images. Sources in the overlap region match the locations of giant molecular clouds seen in CO by Stanford et al. (1990). These similarities suggest that the continuum results largely from star formation. The lack of continuum emission in the tidal tails indicates that recent and ongoing star formation in the Antennae is basically confined to the discs.

The presence of a central H I gas pool along with a modest disc starburst (Gao et al. 2001) and computer simulations (Mihos & Hernquist 1994) suggest that the current starburst may be a weak precursor to a far larger one occurring much later in the merger.

The southern tidal tail contains abundant H I mass (2.5×10^9 M$_\odot$), similar to the galactic discs (2.3×10^9 M$_\odot$), but less concentrated. This tail is connected smoothly to the discs, although *pv* diagrams show a clear breakaway point at 1590 km s^{-1}. Definite H I clumps exist along the length of the tail. It has a substantial H I width of up to $\sim$100 arcsec ($\sim$9 kpc), larger than the optical width. There is no spatial displacement between optical and H I emission. The tip of the southern tail contains a large H I concentration containing $\sim 8.2 \times 10^8$ M$_\odot$ or $\sim$30 per cent of the H I of the tail. At this point the tail also bends sharply in terms of both velocity and shape, and the H I column density is higher by a factor of $\sim$4. This coincides in position with the young tidal dwarf galaxy, observed optically by Mirabel et al. (1992). Dwarf galaxies have previously been produced as a tidal feature by computer simulations, along with pools of material at the ends of tidal arms (Barnes & Hernquist 1992, 1996; Elmegreen et al. 1993), and they have also been observed in other interacting galaxies (e.g. Duc & Mirabel 1994, 1998). Although it is not known that any of the H I pool in the Antennae is associated with the dwarf, it appears likely that they are associated, as seen in the simulations.

The smaller northern tail contains only 1.8×10^8 M$_\odot$ of H I and has no detectable H I connection to the discs, which may be partly as a result of ionization effects suggested by Hibbard et al. (2000). This H I of the tail extends much further lengthwise than its starlight, unlike the southern tail, and it curves towards the west along a faint extension newly detected in our H I data and not visible optically.

While the central H I has broadly similar shape and position to the optical discs, it has a detailed velocity structure and spatial distribution that do not closely resemble those normally observed in discs. The H I appears to have been so kinematically disturbed that it is largely decoupled from the stellar component. The overall velocity range is a high $\sim$640 km s^{-1} and the H I is substantially pooled in the region between the discs, peaking midway between them, unlike optical images. While generally there is only one velocity component along the line of sight, part of the disc H I, close to the southern nucleus, contains two components and thus a high dispersion, up to 150 km s^{-1}.

Comparison of H I mass measurements to previous CO measurements by Wilson et al. (2000) and Gao et al. (2001) gives an estimated molecular-to-atomic gas ratio of $\sim$3:1 for the whole system. The difference between the physical sizes and H I contents of the tails, suggests a difference in the structure or the gas content between the two progenitor galaxies, although asymmetry in the encounter geometry may be responsible.

Our H I images also show the nearby dwarf galaxy ESO 572–G045, which is south-west of the end of the southern tail, and $\sim$91 kpc from the Antennae centre. The H I matches the optical appearance of the galaxy, an edge-on disc $\sim$1 arcmin in width. Using the H I velocity field we estimate a systemic velocity of $\sim$1700 km s^{-1} and a rotational velocity of $\sim$50 km s^{-1}, resulting in a dynamic mass of $\sim 1.74 \times 10^9$ M$_\odot$, compared to an H I mass of $\sim 1.4 \times 10^8$ M$_\odot$. This gives an 8 per cent H I content which appears reasonable. The H I mass of ESO 572–G045 is 3 per cent that of the Antennae. The closeness of the dwarf, and similar velocity, to the adjoining southern tail of the Antennae, indicates that it is a companion galaxy. It appears likely to have been involved in the interaction between the Antennae galaxies, but no major disturbances are observed. Its tidal radius is $\geq$14 kpc, so it is unlikely to be prone to disruption.

ACKNOWLEDGMENTS

We would like to thank both the anonymous referee, and John Hibbard, for their many valuable suggestions, which have been incorporated into this paper. Some figures presented use data from the National Aeronautics and Space Administration (NASA)s *SkyView* facility (http://skyview.gsfc.nasa.gov) located at NASA Goddard Space Flight Center. In particular, use has been made of the Digitised Sky Survey (DSS) images based on photographic data obtained using the UK Schmidt Telescope. Various information used in preparing this paper, was taken from the NASA/IPAC Extragalactic Database (NED), operated by the Jet Propulsion Laboratory, California Institute of Technology, under contract with NASA.

REFERENCES

Amram P., Marcelin M., Boulesteix J., le Coarer E., 1992, A&A, 266, 106
Arp H. C., 1966, ApJS, 14, 1
Arp H. C., 1969, A&A, 3, 418
Barnes J. E., 1988, ApJ, 331, 669
Barnes J. E., Hernquist L., 1992, Nat, 360, 715
Barnes J. E., Hernquist L., 1996, ApJ, 471, 115
Clark B. G., 1980, A&A, 89, 377
Clutton-Brock M., 1972, Ap&SS, 17, 292
Condon J. J., 1983, ApJS, 53, 459
Condon J. J., 1987, ApJS, 65, 485
de Vaucouleurs G., de Vaucouleurs A., Corwin H. G., Jr., Buta R. J., Paturel G., Fouqué P., 1991, Third Reference Catalogue of Bright Galaxies. Springer-Verlag, New York (RC3)

Douglas J. N., Bash F. N., Bozyan F. A., Torrence G. W., Wolfe C., 1996, AJ, 111, 1945
Duc P.-A., Mirabel I. F., 1994, A&A, 289, 83
Duc P.-A., Mirabel I. F., 1998, A&A, 333, 813
Elmegreen B. G., Kaufman M., Thomasson M., 1993, ApJ, 412, 90
Elmegreen D. M., Kaufman M., Brinks E., Elmegreen B. G., Sundin M., 1995a, ApJ, 453, 100
Elmegreen B. G., Sundin M., Kaufman M., Brinks E., Elmegreen B. G., 1995b, ApJ, 453, 139
Fabbiano G., Trinchieri G., 1983, ApJ, 266, L5
Fabbiano G., Schweizer F., Mackie G., 1997, ApJ, 478, 542
Fabbiano G., Zezas A., Murray S. S., 2000, BAAS, 32, 1532
Fischer J. et al., 1996, A&A, 315, L97
Gao Y., Gruendl R. A., Lo K. Y., Lee S.-W., Hwang C. Y., 1998, BAAS, 30, 923
Goa Y., Lo K. Y., Lee S.-W., Lee T.-H., 2001, ApJ, 548, 172
Gioia I. M., Maccacaro T., Schild R. E., Wolter A., Stocke J. T., Morris S. L., Henry J. P., 1990, ApJS, 72, 567
Giovanelli R., Haynes M. P., 1988, in Verschuur G. L., Kellerman K. I., eds, Galactic and Extragalactic Radio Astronomy, 2nd edn. Springer-Verlag, Berlin, p. 522
Hernquist L., 1992, Nat, 360, 105
Hibbard J. E., 1995, PhD thesis, Columbia Univ.
Hibbard J. E., Mihos J. C., 1995, AJ, 110, 140
Hibbard J. E., Vacca W. D., Yun M. S., 2000, AJ, 119, 1130
Hibbard J. E., van Gorkom J. H., 1996, AJ, 111, 655
Högbom J. A., 1974, A&AS, 15, 417
Huchtmeier W. K., Bohnenstengel H. D., 1975, A&A, 41, 477
Hummel E., van der Hulst J. M., 1986, A&A, 155, 151
Karachentsev I. D., Karachentseva V. E., Parnovskij S. L., 1993, Astronomische Nachrichten, 314, 97
Kunze D. et al., 1996, A&A, 315, L101
Maccacaro T., della Ceca R., Gioia I. M., Morris S. L., Stocke J. T., Wolter A., 1991, ApJ, 374, 117
Mahoney J. H., Burke B. F., van der Hulst J. M., 1987, Proc. IAU Symp. 117. p. 94
Mihos J. C., Hernquist L., 1994, ApJ, 431, L9
Mihos J. C., Bothun G. D., Richstone D. O., 1993, ApJ, 418, 82
Mihos J. C., Richstone D. O., Bothun G. D., 1991, ApJ, 377, 72
Minkowski R., 1957, Proc. IAU Symp. 4. Cambridge Univ. Press, Cambridge, p. 107
Mirabel I. F., Lutz D., Maza J., 1991, A&A, 243, 367
Mirabel I. F., Dottori H., Lutz D., 1992, A&A, 256, L19
Mirabel I. F. et al., 1998, A&A, 333, L1
Neff S. G., Ulvestad J. S., 2000, AJ, 120, 670
Nikola T., Genzel R., Herrmann F., Madden S. C., Poglitsch A., Geis N., Townes C. H., Stacey G. J., 1998, ApJ, 504, 749
Parker P. R., 1990, Colliding galaxies: the universe in turmoil. Plenum Press, New York, p. 171
Pisano D. J., Wilcots E. M., 2000, MNRAS, 319, 821
Read A. M., Ponman T. J., Wolstencroft R. D., 1995, MNRAS, 277, 397
Roberts M. S., 1975, in Sandage A., Sandage M., Kristian J., eds, Galaxies and the Universe. Univ. Chicago Press, Chicago, p. 309
Rubin V. C., Ford W. K., D'Odorico S., 1970, ApJ, 160, 801
Sanders D. B., Mirabel I. F., 1985, ApJ, 298, L31
Sanders D. B., Mirabel I. F., 1996, ARA&A, 34, 749
Sansom A. E., Dotani T., Okada K., Yamashita A., Fabbiano G., 1996, MNRAS, 281, 48
Sault R. J., Teuben P. J., Wright M. C. H., 1995, in Shaw R. A., Payne H. E., Hayes J. J. E., eds, ASP Conf. Ser. Vol. 77, Astronomical Data Analysis Software and Systems IV. Astron Soc. Pac., San Francisco, p. 433
Schweizer F., 1978, in Berkhuijsen E. M., Wielebinski R., eds, Proc. IAU Symp. 77, Structure and Properties of Nearby Galaxies. Reidel, Dordrecht, p. 279
Shapley H., Paraskevopoulos J. S., 1940, Proc. Nat. Acad. Sci., 26, 31
Stanford S. A., Sargent A. I., Sanders D. B., Scoville N. Z., 1990, ApJ, 349, 492
Steer D. G., Dewdney P. E., Ito M. R., 1984, A&A, 137, 159
Stocke J. T. et al., 1991, ApJS, 76, 813
Toomre A., 1977, in Tinsky B. M., Larson R. B., eds, Evolution of Galaxies and Stellar Populations. Yale Univ. Observatory, New Haven, p. 401
Toomre A., Toomre J., 1972, ApJ, 178, 623
van der Hulst J. M., 1979, A&A, 71, 131
Vigroux L. et al., 1996, A&A, 315, L93
Whitmore B. C., Schweizer F., 1995, AJ, 109, 960
Whitmore B. C., Zhang Q., Leitherer C., Fall S. M., Schweizer F., Miller B. W., 1999, AJ, 118, 1551
Wilson C. D., Scoville N., Madden S. C., Charmandaris V., 2000, ApJ, 542, 120
Young J. S. et al., 1995, ApJS, 98, 219

This paper has been typeset from a TEX/LATEX file prepared by the author.